Particle Pile-ups and Planetesimal Formation

Andrew N. Youdin & Eugene I. Chiang

Department of Astronomy, University of California, Berkeley, CA 94720

ABSTRACT

Solid particles in protoplanetary disks that are sufficiently super-solar in metallicity overcome turbulence generated by vertical shear to gravitationally condense into planetesimals. Super-solar metallicities result if solid particles pile up as they migrate starward as a result of aerodynamic drag. Previous analyses of aerodynamic drift rates that account for mean flow differences between gas and particles yield particle pile-ups. We improve on these studies not only by accounting for the collective inertia of solids relative to that of gas, but also by including the transport of angular momentum by turbulent stresses within the particle layer. These turbulent stresses are derived in a physically self-consistent manner from the structure of marginally Kelvin-Helmholtz turbulent flows. They are not calculated using the usual plate drag formulae, whose use we explain is inappropriate. Accounting for the relative inertia of solids to gas retards, but does not prevent, particle pile-ups, and generates more spatially extended regions of metal enrichment. Turbulent transport hastens pile-ups. We conclude that particle pile-up is a robust outcome in sufficiently passive protoplanetary disks. Connections to observations of circumstellar disks, including the Kuiper Belt, and the architectures of planetary systems are made.

Subject headings: planetary systems: protoplanetary disks — planets and satellites: formation — turbulence — methods: numerical

1. Introduction

The formation of planetesimals by gravitational instability within dense particle layers in circumstellar disks is an appealing alternative to collisional sticking of dust aggregates (Youdin & Shu 2002, hereafter YS02, and references therein). In one fell swoop, gravity promises to assemble sand-sized or smaller solids into kilometer-sized agglomerates.

For gravitational instability to operate, two main requirements must be met. First, the disk must be sufficiently passive; turbulent velocity fluctuations in disk gas must be small

enough to allow solids to gravitationally settle toward the midplane. Kelvin-Helmholtz turbulence generated by vertical shear within the stratified particle layer threatens to violate this requirement (Cuzzi et al. 1993; Weidenschilling 1995). Such turbulence, however, can entrain only a finite amount of solids. Thus, a second requirement for gravitational instability, first explored by Sekiya (1998), is that the surface density of solids relative to that of gas, $\Sigma_{\rm p}/\Sigma_{\rm g}$, must exceed a critical threshold, $\Sigma_{\rm p,cr}/\Sigma_{\rm g}$. Within the minimum-mass solar nebula (MMSN), $\Sigma_{\rm p,cr}/\Sigma_{\rm g}$ lies $\sim$5 — 20 times above the solar value of $\Sigma_{\rm p}/\Sigma_{\rm g} \sim 5 \times 10^{-3}$.

Many possibilities exist for achieving this enhancement of metallicity, including the return of condensed material to an accretion disk from a bipolar outflow and removal of dust-depleted gas in disk surface layers by magnetic accretion, photoevaporation, or entrainment within a stellar wind. YS02 discuss the origins and merits of these possibilities. They highlight a promising and natural enrichment mechanism that arises from simple aerodynamic drag. Solid particles rotate about the central star faster than does ambient gas because the latter is more sensitive to pressure gradients that are (usually) directed radially outward. This difference in mean flow velocities causes particles to be frictionally dragged by gas. Such drag induces orbital decay. By applying the Epstein aerodynamic drag law to millimeter-sized solids in the MMSN, YS02 conclude that as particles drift relative to gas toward the central star, they pile up: local enhancements of more than an order-of-magnitude in the particle surface density (metallicity) occur at small stellocentric radii.

The Epstein drag law applies when relative velocities, $v_{\rm rel}$, between a solid particle and surrounding gas are less than the gas sound speed, $c_{\rm g}$, and when the particle radius, a, is smaller than the gaseous mean free path, λ. These conditions are satisfied for particles having $a \lesssim 1\,(r/{\rm AU})^{2.75}$ cm in the MMSN, where r is the stellocentric distance. The Epstein drag force on a spherical particle reads

$$D_{\rm Ep} = \frac{4\pi}{3}\rho_{\rm g}c_{\rm g}v_{\rm rel}a^2\,, \tag{1}$$

where $\rho_{\rm g}$ is the mass density of gas. YS02 find that millimeter-sized particles pile up to the point where their density exceeds the Roche density in $\sim10^5$ yr, fast enough to occur within disk lifetimes ($\sim10^7$ yr).

Recently, Weidenschilling (2003) has argued that metallicity enhancement is unlikely because Epstein-type drag, as described above, inadequately describes the forces on particles. Since the timescale for a particle to settle vertically toward the midplane is shorter than the timescale for a particle to drift radially by Epstein drag [by a factor of order $\eta \sim 10^{-3}(r/{\rm AU})^{1/2}$; see the next section], particles settle vertically into states of marginal Kelvin-Helmholtz turbulence (see Sekiya 1998) before drifting appreciably in the radial direction. Such turbulence exerts additional stresses on particles, stresses that are not accounted for by

Epstein drag; radial drift rates could, in principle, be altered significantly. Weidenschilling (2003) proceeds by assuming, as have other authors in different contexts (e.g., Goldreich & Ward 1973; Goodman & Pindor 2000, hereafter GP00), that this extra turbulent stress can be modeled as "plate drag": the turbulent stress on the particle layer is taken to be akin to the turbulent stress on a solid, rigid plate that is dragged through gas. The turbulent stresses so prescribed still induce inward radial drift of solids relative to gas, but the new, equilibrium drift velocities scale with stellocentric distance in such a way that particle pile-ups and metallicity enhancements do not occur in the MMSN.

GP00 also employ the plate drag prescription to study the local, two dimensional dynamics of the turbulent dust sheet. They discover an instability that causes in-plane perturbations to grow over the local dynamical time. This instability was not recovered by Weidenschilling (2003) because the latter solved for the equilibrium state, in which unbalanced gravitational forces on the dust layer match exactly the drag force; perturbations in radial momentum about this state were not considered.[1]

Our purpose here is to discard the usual plate drag prescription in favor of a self-consistent calculation of turbulent stresses based on the structure of the stratified particle layer. The essence of our approach is to solve for the turbulent diffusivity necessary to keep solids mixed vertically in the Kelvin-Helmholtz turbulent state, and then to employ this diffusivity in calculating rates of angular momentum transport. We find that the inclusion of turbulent stresses promotes local metal enrichment as particles accrete toward the central star; particles pile up radially more quickly with such stresses than without them.

Our analysis below is restricted to millimeter-sized particles, though it can be extended to govern smaller sizes. As long as the Schmidt numbers of individual particles are nearly unity (see §2.2.2), the particles are well entrained in the gas and we may model the gas and particles as a single fluid. One millimeter is an interesting size regime from a number of perspectives. First, insofar as we would like to form planetesimals from seed particles that are as small as possible, with minimum recourse to collisional sticking, millimeter (or smaller) scales are more interesting to us than the meter scales that concern other works such as GP00. Second, collisional sticking might stall at sizes of a few millimeters, since relative velocities between particles tend to increase with increasing particle size, and relative velocities that are too high result in shattering of particle aggregates rather than sticking. Current consensus tells us that the threshold velocity that divides sticking from shattering is ~ 1 m s^{-1} and that the corresponding maximum particle size generated by particle-particle collisions is ~ 1 cm (Weidenschilling & Cuzzi 1993; Blum & Wurm 2000; Wurm, Blum, & Colwell 2001;

---

[1] These equilibrium states are referred to as "constant states" by GP00.

Chiang 2003). Third, modelling of millimeter-wave spectra of T Tauri and Herbig Ae star-disk systems offers evidence in favor of millimeter-sized grains dominating the particle mass near disk midplanes; the evidence is critically reviewed by Chiang (2003). Fourth, millimeter sizes characterize chondrules, the dominant constituent of the most primitive meteorites.

In §2 we describe aerodynamic drift mechanisms for solids. Epstein drag is recapitulated in §2.1, while turbulent stresses are considered in §2.2. We review the plate drag prescription in §2.2.1 and introduce our new, self-consistent approach for calculating the transport of angular momentum by Kelvin-Helmholtz turbulence in §2.2.2. In §3 we apply our theory to a global simulation of the evolution of Σ_p and demonstrate how particles pile up robustly. In §4 we argue more pointedly why our treatment of turbulent drag represents an improvement over the usual plate drag approximation. Concluding remarks are made in §5. Related discussions of the character and strength of turbulence in planetesimal forming disks are relegated to the appendices.

2. Mechanisms for Radial Drift of Solids

2.1. Epstein Drag

Gas in protoplanetary disks rotates at speeds lower than the Keplerian speed, v_K, by an amount $\sim \eta v_K$, where

$$\eta \equiv -\frac{\partial P_g / \partial \ln r}{2\rho_g v_K^2} \approx \left(\frac{c_g}{v_K}\right)^2 \tag{2}$$

is a dimensionless measure of radial pressure support and P_g is the gas pressure. Typical models of the MMSN are characterized by $\eta \sim 10^{-3}(r/\mathrm{AU})^{1/2}$.

The Epstein aerodynamic drag law [equation (1)] implies that the stopping time of a particle of mass m_p moving relative to gas is

$$t_{\mathrm{stop}} \equiv \frac{m_p v_{\mathrm{rel}}}{D_{\mathrm{Ep}}} = \frac{\rho_s a}{\rho_g c_g} . \tag{3}$$

For a particle of internal density $\rho_s = 3$ g/cm^3 and radius $a = 1$ mm, the stopping time is likely shorter than the disk rotation period, $r/v_K = 1/\Omega$; to wit,

$$\Omega t_{\mathrm{stop}} \sim 10^{-4} \left(\frac{r}{\mathrm{AU}}\right)^p , \tag{4}$$

where the index p describes the fall-off of gas surface density with distance,

$$\Sigma_{\mathrm{g}} \propto r^{-p} \,. \tag{5}$$

If $\Omega t_{\mathrm{stop}} \ll 1$, gas and solids rotate at nearly—to order $\eta(\Omega t_{\mathrm{stop}})^2$—the same azimuthal velocity,

$$v_{\phi} = \left[1 - \eta \frac{\rho_{\mathrm{g}}}{\rho_{\mathrm{g}} + \rho_{\mathrm{p}}(z)} \right] v_K \tag{6}$$

(Nakagawa et al. 1986). We make explicit the dependence of particle mass density, ρ_{p}, on vertical height, z, above the midplane because vertical stratification of solids provides the only significant source of vertical shear, $\partial v_{\phi}/\partial z$. This shear, in turn, drives Kelvin-Helmholtz turbulence.

The radial drift speed of an individual particle can be derived via force balance in the radial and azimuthal directions (see, e.g., Goldreich & Ward 1973). Under the approximation that the azimuthal velocity of the particle equals the azimuthal velocity of the gas, the equation for radial force balance yields for the radial drift speed:

$$v_{\mathrm{Ep,ind}} = 2\eta \Omega t_{\mathrm{stop}} v_K \,. \tag{7}$$

The convention in this paper is that radially inward velocities are positive. Corrections to this expression are higher order in Ωt_{stop}. When the inertia of a collection of solids is taken into account, equation (7) becomes

$$v_{\mathrm{Ep}} = \left(\frac{\rho_{\mathrm{g}}}{\rho} \right)^2 v_{\mathrm{Ep,ind}}, \tag{8}$$

which is always smaller than $v_{\mathrm{Ep,ind}}$ because $\rho = \rho_{\mathrm{p}} + \rho_{\mathrm{g}}$ (Nakagawa et al. 1986). We refer to this dampening of the drift rate due to the collective inertia of the solids as the "inertial slow-down" effect. Note that while we have subscripted our velocities in equations (7) and (8) by "Ep" to denote the Epstein drag law, the form of the right-hand-side of equation (7) and the correction factor of ρ_{g}/ρ in equation (8) are independent of the drag law employed (e.g., for $a > \lambda$, the appropriate drag law is due to Stokes: $D \propto a\lambda c_{\mathrm{g}} v_{\mathrm{rel}}$). The same independence does not apply to the explicit form of t_{stop}, which is given for the specific case of Epstein drag on the far right-hand side of equation (3).

Particle pile-ups occur if the mass accretion rate in particles decreases with decreasing r at fixed time. Define

$$\Sigma_{\mathrm{p}} \propto r^{-n} \tag{9}$$

to be the surface density of solids. Further define the radial drift rate of solids to be, in general,

$$v_r \propto r^d . \tag{10}$$

Then the mass accretion rate in particles scales as

$$\Sigma_{\mathrm{p}} r v_r \propto r^E , \tag{11}$$

where $E = d - n + 1$. If $E > 0$, then accretion results in particle pile-ups and local metal enrichment.

For the specific case of Epstein drag,

$$d_{\mathrm{Ep}} = \frac{1}{2} - q + p , \tag{12}$$

$$E_{\mathrm{Ep}} = \frac{3}{2} + p - n - q , \tag{13}$$

where the small inertial slow-down correction has been neglected. Here q describes the fall-off of midplane gas temperature with distance,

$$T \propto r^{-q} . \tag{14}$$

Reasonable values of q (see, e.g., Chiang & Goldreich 1997) span the range of 0.43–0.75. If the disk begins in a well-mixed state for which $p = n$, then $E_{\mathrm{Ep}} \gtrsim 1$ initially and particles pile up as they accrete. Pile-ups cannot occur everywhere for all time. When a realistic disk with finite outer radius is considered, Σ_{p} at a fixed r will grow until particles at the outer radius drift past r.

Figure 1 portrays the particle flux from Epstein drag,

$$f_{\mathrm{Ep}} = \rho_{\mathrm{p}} v_{\mathrm{Ep}} , \tag{15}$$

as a function of z for particles having $a = 1$ mm and $\rho_{\mathrm{s}} = 3$ g/cm^3 at $r = 1$ AU in Hayashi's (1981) model of the MMSN. We refer to this background nebular model hereafter as "model H." See YS02 for details of all nebular models used in this paper. Figure 2 is analogous to Figure 1, except that $\Sigma_{\mathrm{p}}/\Sigma_{\mathrm{g}}$ is set to near the saturation limit, $\Sigma_{\mathrm{p}}/\Sigma_{\mathrm{g}} = 0.99\Sigma_{\mathrm{p,cr}}/\Sigma_{\mathrm{g}}$; for the case of model H at $r = 1$ AU, this represents a factor of ~ 17 enhancement over solar metallicity. Distributions of particle density with height are computed using the model of Sekiya (1998) for which the Richardson number equals 1/4 everywhere. The fluxes are scaled to $\rho_{\mathrm{g}} v_{\mathrm{Ep,ind}}$, which is independent of ρ_{p}.
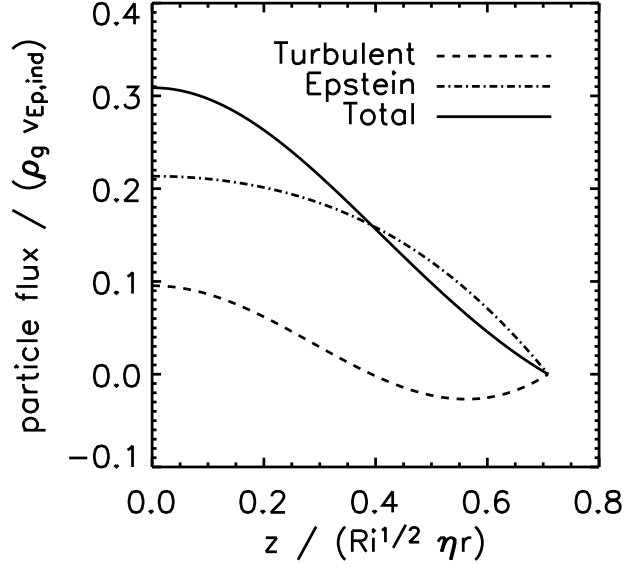
Fig. 1.— Radial particle fluxes from turbulent stresses, Epstein drag, and their sum vs. height above the midplane for millimeter-sized particles in model H at $r \sim 1$ AU. The vertically integrated abundance of chondrule-like particles is fixed at its cosmic value. Positive fluxes represent inflow.

Before discussing the turbulent contribution to radial drift rates of solids, we prove that vertical settling of particles into the Kelvin-Helmholtz turbulent state occurs well before particles drift radially inward by Epstein drag. The timescale for vertical settling equals

$$t_{\text{sett}} \sim \frac{H_{\text{g}}}{\Omega^2 z t_{\text{stop}}} \sim \frac{1}{\Omega^2 t_{\text{stop}}}, \tag{16}$$

where $H_{\text{g}} = c_{\text{g}}/\Omega$ equals the vertical scale height of the gas, $\Omega^2 z$ equals the vertical component of stellar gravity, and we have set $z = H_{\text{g}}$ in the last equality in working to order-of-magnitude. The timescale for radial drift equals

$$t_{\text{Ep}} \sim \frac{r}{v_{\text{Ep}}}. \tag{17}$$

Substituting (7) and (8) into (17) reveals immediately that $t_{\text{sett}}/t_{\text{Ep}} \sim \eta(\rho_{\text{g}}/\rho)^2 \ll 1$.

2.2. Turbulent Stresses in Stratified Disks

Forces exerted by gas turbulence are often modeled using the symmetric pressure tensor, **P**. In dynamical equilibrium, the advective transport of angular momentum balances the torque exerted by turbulent pressure fluctuations; to wit,

$$v_{\rm r,turb}\frac{\partial \Omega r^2}{\partial r} = -\frac{r}{\rho}\left(\frac{1}{r^2}\frac{\partial r^2 P_{r\phi}}{\partial r} + \frac{1}{r}\frac{\partial P_{\phi\phi}}{\partial \phi} + \frac{\partial P_{z\phi}}{\partial z}\right) ,\tag{18}$$

where $v_{\rm r,turb}$ is the radial accretion velocity induced by turbulent stresses and (r,ϕ,z) are the usual cylindrical coordinates. Again, $v_{\rm r,turb} > 0$ for radially inward accretion. The term proportional to $P_{r\phi}$ dominates in active accretion disks that are rendered turbulent by, e.g., magneto-rotational instability (Balbus & Hawley 1991) or gravitational instability (Gammie 2001). The disks considered here derive their turbulence from vertical shear instabilities, so that we set $P_{r\phi} = 0$ (see the appendices for quantitative justification). We further assume that the disk is axisymmetric so that $\partial P_{\phi\phi}/\partial \phi = 0$. Equation (18) then reduces to

$$\frac{v_{\rm r,turb}}{r}\frac{\partial \Omega r^2}{\partial r} = -\frac{1}{\rho}\frac{\partial P_{z\phi}}{\partial z} .\tag{19}$$

How can one model $P_{z\phi}$ in turbulent particle disks? In the next two subsections, we examine two prescriptions: one based on the conventional "plate drag" *Ansatz*, and a second rooted in the physics of stratified particle layers.

2.2.1. The Plate Drag Approximation

We review the "plate drag" treatment of turbulent stresses to connect to previous works [e.g., Goldreich & Ward (1973); GP00; Weidenschilling (2003)] and to contrast it with the new approach we champion in the next section §2.2.2. Section 4 criticizes the plate drag approximation more directly.

Users of the plate drag prescription do not resolve the stress, $P_{z\phi}$, as a function of z. Instead, $P_{z\phi}$ is vertically averaged and utilized to calculate an average accretion velocity. Averaging equation (19) over z yields

$$\frac{\langle v_{\rm r,turb}\rangle}{r}\frac{\partial \Omega r^2}{\partial r} = \frac{S}{\Sigma(H_{\rm p})} ,\tag{20}$$

where $\langle \rangle$ denotes a density-weighted average, $\Sigma(H_{\rm p})$ is the surface density of solids and gas

within the particle layer of half-thickness H_{p}, and

$$S = 2 \int_0^{H_{\mathrm{p}}} \frac{\partial P_{z\phi}}{\partial z} dz = 2 P_{z\phi}(z = H_{\mathrm{p}}). \tag{21}$$

We have used the fact that $P_{z\phi}$ vanishes for $|z| > H_{\mathrm{p}}$ and is an odd function of z. The heart of the plate drag prescription lies in setting the drag force per unit area, S, equal to

$$S = -\rho_{\mathrm{g}} \frac{(\Delta v_\phi)^2}{\mathrm{Re}^*}, \tag{22}$$

where $\Delta v_\phi \approx \eta v_K$ is the characteristic azimuthal velocity difference between a dense particle-dominated midplane and overlying particle-free gas.

Prescription (22) is useful only to the extent that Re^* and any radial variations in this quantity are known. Goldreich & Ward (1973) assume that $\mathrm{Re}^* = 500$, citing an analysis of tidal boundary layers on the Earth's ocean floor. More recently, Cuzzi et al. (1993) and Dobrovolskis et al. (1999) obtain values of Re^* ranging anywhere from 20 to 180 by using (the square of) three experimentally determined boundary lengths. Whether the results of these terrestrial-scale experiments can be extrapolated to astronomical settings has not been rigorously demonstrated.

Insertion of (22) into (20) yields the equilibrium accretion velocity

$$\langle v_{\mathrm{r,turb}} \rangle = v_{\mathrm{plate}} = \frac{2 \rho_g \eta^2 \Omega r^2}{\Sigma_{\mathrm{p}} \mathrm{Re}^*}, \tag{23}$$

where we have replaced $\Sigma(H_{\mathrm{p}})$ with Σ_{p} for consistency with other authors (although this replacement is strictly valid only if $\rho_{\mathrm{p}} \gg \rho_{\mathrm{g}}$) and for ease when making analytic scalings. Equation (23) implies that the indices d and E introduced in §2.1 take the values $d_{\mathrm{plate}} = 1 - 3q/2 - p + n$ and $E_{\mathrm{plate}} = 2 - 3q/2 - p$, respectively, if we assume that Re^* is spatially constant.

In model H, $p = n = 3/2$ and $q = 1/2$. Then $E_{\mathrm{plate}} = -1/4$; solids drain from the disk onto the star and do not pile up. This is the result obtained by Weidenschilling (2003), who went on to show that adding the particle flux due to Epstein drag to that due to plate drag caused metal enhancement and depletion effects to cancel nearly exactly. We offer two comments regarding these results. The first is that whether the equilibrium solutions yield particle pile-ups is highly model-dependent. For example, an initial surface density profile for which $p = n = 1$ and $q = 1/2$ gives $E_{\mathrm{plate}} = 1/4$.[2] Our second comment is that such

---

[2] For particles larger than the gas mean free path, the drag law is due to Stokes (see §1), and $E = -q/2 - n$,
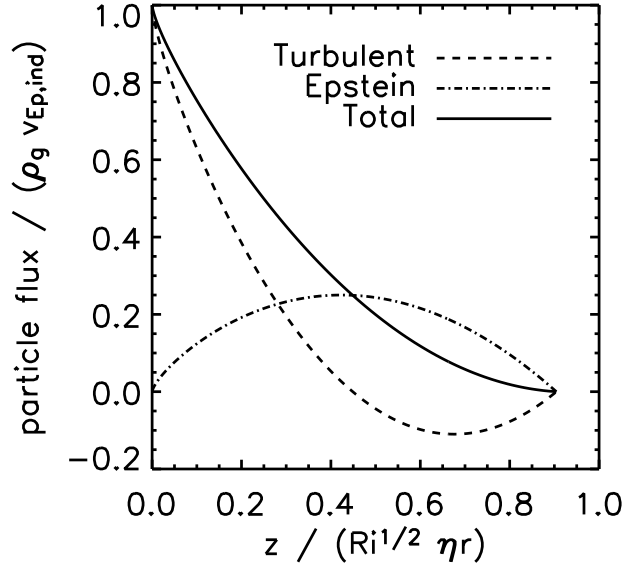
Fig. 2.— Same as Figure 1, except the surface density of solids has been increased to near the saturation limit: $\Sigma_{\rm p} = 0.99\Sigma_{\rm p,cr}$.

equilibrium solutions neglect the instability discovered by GP00, which yields metallicity enhancement on dynamical timescales when the plate drag prescription applies.

In the next section we derive an alternative prescription for turbulent stresses based on the structure of Kelvin-Helmholtz turbulent flows.

2.2.2.   A Self-Consistent Description of Turbulent Stresses

Proceeding from equation (19), we express the turbulent stress,

$$P_{z\phi} = \rho\nu_z\frac{\partial v_\phi}{\partial z}\,, \tag{24}$$

in terms of a momentum diffusivity (viscosity), ν_z, which controls the efficiency of vertical mixing of azimuthal momentum. This same diffusivity also characterizes vertical mixing of particles; the ratio of the diffusivity of momentum to that of particles is the Schmidt

---

i.e., no pile-up for decreasing temperature and density profiles. Loss of such large particles to accretion onto the star is another reason why we restrict ourselves to the millimeter sizes.

number, Sc; it is unity for the small particles considered here for which $\Omega t_{\mathrm{stop}} \ll 1$ and that are entrained in all but the smallest turbulent eddies (Cuzzi et al. 1993). Given the equivalence of these diffusivities, we may derive ν_z from vertical profiles of particle density as computed by Sekiya (1998). Our procedure is developed as follows.

The equilibrium distribution of particle density, $\rho_{\mathrm{p}}(z)$, reflects a detailed balance between turbulent diffusion and gravitational settling. The speed of upward particle diffusion is given by

$$w_{\mathrm{diff}} = -\nu_z \frac{\partial \ln \rho_{\mathrm{p}}}{\partial z}, \tag{25}$$

while the downward vertical settling speed is nearly terminal,

$$w_{\mathrm{sett}} = -\Omega^2 z t_{\mathrm{stop}}. \tag{26}$$

Vertical flux balance, $w_{\mathrm{diff}} + w_{\mathrm{sett}} = 0$, allows us to calculate the turbulent viscosity in terms of known quantities:

$$\nu_z = -\frac{\Omega^2 t_{\mathrm{stop}} z}{\partial \ln \rho_{\mathrm{p}}/\partial z}. \tag{27}$$

Note that the local viscosity increases with stopping time and with height above the midplane. More vigorous turbulence is required to keep larger particles aloft and at greater distances above the midplane where the vertical component of stellar gravity is stronger. In addition, strong gradients in particle density survive only in regions of low viscosity.

We use (6) and (27) in (24) to calculate the relevant component of the stress tensor as

$$P_{z\phi} \approx -\eta r z \Omega^3 t_{\mathrm{stop}} \frac{\rho_{\mathrm{g}}}{\rho} \rho_{\mathrm{p}}. \tag{28}$$

Insertion of (28) into (19) yields the resulting equilibrium drift speed,

$$v_{\mathrm{r,turb}} \approx -\frac{2}{\rho \Omega} \frac{\partial P_{z\phi}}{\partial z} \approx v_{\mathrm{Ep,ind}} \frac{\rho_{\mathrm{g}}}{\rho} \frac{\partial}{\partial z} \left(\frac{\rho_{\mathrm{p}}}{\rho} z \right). \tag{29}$$

Since the gas scale height, H_{g}, is larger than the particle scale height ($H_{\mathrm{p}}/H_{\mathrm{g}} \sim \sqrt{\eta} \ll 1$), we have ignored vertical gradients in gas properties in writing equation (29). Note that $v_{\mathrm{r,turb}}$ differs from the Epstein drag rate only via the shapes of the gas and particle density profiles. Since $\rho_{\mathrm{p}} z/\rho$ is antisymmetric about the midplane and decreases near the top of the particle layer (as $\rho_{\mathrm{p}} \to 0$), equation (29) implies radial inflow near the midplane and radial outflow at greater heights.

Note further that with the exception of the last step in equation (29), our treatment in this section does not depend on the validity of the Epstein drag law; the only requirement

is that the Schmidt number be unity, or equivalently that particles be small enough that $\Omega t_{\text{stop}} \ll 1$. Strict adoption of the results in Cuzzi et al. (1993)—see, in particular, their Figure 2—tells us that the Schmidt number for millimeter-sized particles in a Hayashi nebula varies from $\text{Sc} = 1$ inside $r = 1$ AU to $\text{Sc} = 10$ at $r = 100$ AU. For particle sizes $a \gtrsim 1$ cm, the Schmidt number varies more strongly with r. Unfortunately, while it is true asymptotically that $\Omega t_{\text{stop}} \ll 1$ implies $\text{Sc} = 1$, the precise values for Sc cited in Cuzzi et al. (1993) depend on poorly constrained dimensionless numbers; see their sections 2.2 and 2.3. We work, for simplicity, under the assumption of constant $\text{Sc} \approx 1$; despite the uncertainties involved, even this latter requirement could be relaxed by introducing a spatially variable Schmidt number.

The equilibrium particle mass flux due to turbulent stresses,

$$f_{\text{turb}} = \rho_{\text{p}} v_{\text{r,turb}} \,, \tag{30}$$

is plotted in Figures 1 and 2 for the cases of solar and super-solar metallicities, together with the previously discussed fluxes due to Epstein drag. In the case of solar metallicity, the turbulent flux increases the midplane flux by $\sim 50\%$. The relative importance of turbulent fluxes increases with increasing metallicity; for the metal-rich case displayed in Figure 2, turbulent fluxes dominate near the midplane.

It appears that turbulent stresses enhance the mass accretion rates due to Epstein drag. We proceed to execute global simulations of radial drift to investigate the possibility of particle pile-ups in the presence of both Epstein drag and turbulent stresses.

3. Global Evolution

We solve the mass continuity equation in the radial direction. Integrated over height, the continuity equation reads

$$\frac{\partial \Sigma_{\text{p}}}{\partial t} = \frac{1}{r} \frac{\partial}{\partial r} (rF) \,, \tag{31}$$

where the total particle flux equals

$$F = F_{\text{Ep}} + F_{\text{turb}} = \int_{-H_{\text{p}}}^{H_{\text{p}}} (f_{\text{Ep}} + f_{\text{turb}}) \, dz \,. \tag{32}$$

As before, we assume an axially symmetric disk that is everywhere in a state of marginal Kelvin-Helmholtz turbulence.

The integrals of flux over height can be computed analytically for the Sekiya models once the midplane density, $\rho_{\text{p}}(0)$, is known. One finds

$$\frac{F_{\text{Ep}}}{\rho_{\text{g}} \eta r v_{\text{Ep,ind}}} = \left[u_0^2 \left(\frac{3}{2} \chi - 1 \right) + \chi \psi^2 \right] \mathcal{L} - \left(1 + \frac{2}{3} u_0^2 - 3\chi + \frac{11}{6} \chi^2 \right) \mathcal{R} \tag{33}$$

$$\frac{F_{\text{turb}}}{\rho_{\text{g}}\eta r v_{\text{Ep,ind}}} = \frac{1}{12}\left\{\left[4u_0^2 + \chi(11\chi - 9)\right]\mathcal{R} + 3\left[u_0^2(1 - 3\chi) - 2\psi\chi^2\right]\mathcal{L}\right\} \tag{34}$$

where

$$u_0 \equiv \frac{\rho_{\text{g}}}{\rho_{\text{g}} + \rho_{\text{p}}(0)} + \psi, \tag{35}$$

$$\chi \equiv 1 + \psi \equiv 1 + 4\pi G\rho_{\text{g}}/\Omega^2, \tag{36}$$

$$\mathcal{R} \equiv \sqrt{\chi^2 - u_0^2}, \tag{37}$$

$$\mathcal{L} \equiv \ln\left(\frac{\chi + \mathcal{R}}{u_0}\right). \tag{38}$$

Although cumbersome, these exact expressions permit greater accuracy and computational efficiency over direct numerical integration.

Input parameters and boundary values for our first-order partial differential equation (31) are as follows. Particles have $\rho_{\text{s}} = 3$ g/cm^3 and $a = 1$ mm. The gas disk obeys fixed power laws [equations (5) and (14)] with specific values for indices and normalizations taken from either model H or model Af (see YS02). The initial surface density profile for solids is scaled to that of gas but with an exponential cut-off at large radius, $\Sigma_{\text{p}}(r, t = 0) = \Sigma_{\text{g}}\exp(-x^2)/200$, where $x = r/(200 \text{ AU})$. The choice of $\Sigma_{\text{p}}/\Sigma_{\text{g}} = 5 \times 10^{-3}$ at $x \ll 1$ assumes that only refractory material at solar abundances has condensed; inclusion of ices would enlarge $\Sigma_{\text{p}}/\Sigma_{\text{g}}$. Our outer boundary condition imposes a "lid" around the disk's outer edge, $F(r_{\text{out}} = 350 \text{ AU}) = 0$. We note that an inflow boundary condition, $\partial F/\partial r =$ constant at $r = r_{\text{out}}$, yields nearly identical results because of the exponential cutoff in Σ_{p}. No boundary condition is required at the inner boundary, $r_{\text{in}} = 0.5$ AU, where material leaves the grid.

3.1. Numerical Techniques

As in all advection problems, we must obey the Courant condition. The time step, Δt, must be smaller than the time for the flow, at speed v_r, to pass from one grid point to the next; i.e., the Courant number Co $\equiv \Delta t v_r/\Delta r < 1$ everywhere, where Δr is the grid spacing. The computational cost is dominated by regions with small $\Delta r/v$. Since $v_r \propto r^d$ roughly, the most efficient (non-adaptive) grid spacing is $\Delta r \propto r^d$ so that we can fix Co $= 0.5$ everywhere. Such a grid, which is logarithmic only for $d = 1$, is generated by the recursion relation:

$$r_{j+1} = r_j(1 + \epsilon r_j^{d-1}), \tag{39}$$

where the index j labels the gridpoint and ϵ is a constant based on the number of radial gridpoints, N_r, and the desired range of r-values. This same grid works for all times because

we calculate Co using $v_r = v_{\text{Ep,ind}}$, so that d depends only on time-independent gas properties; see equation (12). Evolutionary increases in particle density only act to decrease the flow speed, which poses no danger of violating the Courant condition.

We found (see Figure 5) that setting $N_r = 1000$ permitted fast integration with more than sufficient accuracy. The finite difference technique for the solution of (31) is explicit, upwind, forward in time, and first order (see Press et al. 1992, chap. 19.1). This simple technique proved convergent, stable, and accurate.

Analytic evaluation of the vertically integrated fluxes [equations (33) and (34)] requires that we first obtain $\rho_{\text{p}}(z = 0)$ given the current value of Σ_{p} at every radial gridpoint. To this end, we employ a non-linear root finder based on an optimized Müller's method. The root-finding algorithm requires good initial guesses; it is the rate-limiting step in our simulation.

We halt the simulation once $\Sigma_{\text{p}} = \Sigma_{\text{p,cr}}$ anywhere. At this point, $\rho_{\text{p}}(0)$ becomes formally infinite, and gravitational instability ensues. One can imagine continuing the simulation by removing any excess surface density above $\Sigma_{\text{p,cr}}$; the surface density of agglomerated planetesimals could then be tracked as a function of position and time.

3.2. Results

We now come to our main result, the evolution of $\Sigma_{\text{p}}(r, t)$ subject to Epstein drag and turbulent stresses when the vertical density profiles, $\rho_{\text{p}}(z)$, are supplied by models of Sekiya (1998). These results improve on the analytic models of YS02 who considered only Epstein drag and ignored both the inertial slow-down effect and turbulent stresses.

Figure 3 showcases the evolution of particle surface density in model H under two cases: one in which only Epstein drag (corrected for inertial slow-down) is included, and a second in which both Epstein drag and turbulent transport of angular momentum are included. Pile-ups of surface density occur whether or not turbulent stresses are included in the calculation. Turbulent stresses accelerate the inflow and promote particle pile-ups. The simulation including turbulent stresses was halted after 5.3×10^5 yrs when $\Sigma_{\text{p}} > \Sigma_{\text{p,cr}}$ at $r = 2.5$ AU. To obtain saturation densities at larger stellocentric radii, one could start with a larger disk or a more metal-rich disk in which more solids could be provided by condensible ices.

For model H, planetesimal formation is first triggered at the outer boundary or "cliff edge" of the shrinking disk of solids. This behavior is explained as follows. If the actual particle surface density flattens from its initial profile—i.e., if $|d \ln \Sigma_{\text{p}}/d \ln r| < |p|$—then
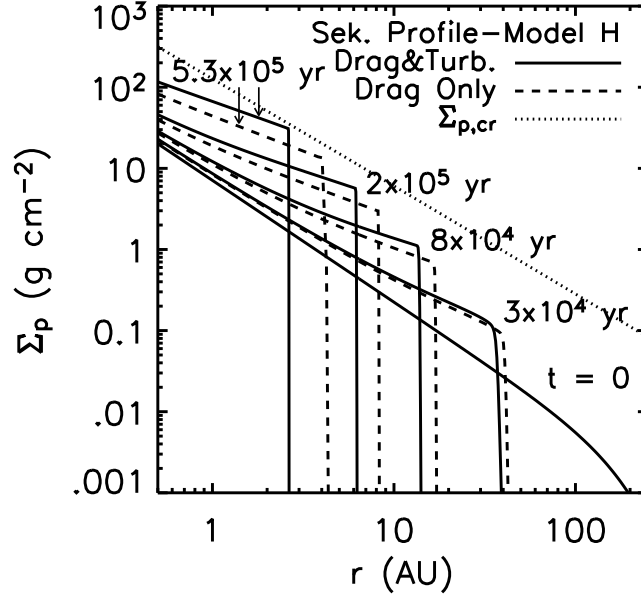
Fig. 3.— Evolution of the surface density, Σ_p, of millimeter-sized particles with time for model H using 10^3 gridpoints. Solid lines include both Epstein drag and turbulent stresses as sources of radial drift; dashed lines ignore turbulent stresses for comparison. In both cases, Σ_p grows and its profile flattens with time as the particle disk contracts radially. Gravitational instability is first triggered when Σ_p crosses $\Sigma_{p,cr}$ at the shrinking outer edge, here $r \sim 2.5$ AU.

Σ_p will first exceed $\Sigma_{p,cr}$ at the outer boundary of the accreting disk of particles. Whether the radial profile of particle surface density flattens depends on how the timescale for local density amplification, $\Sigma_p/\dot{\Sigma}_p$, scales with r. Equation (31) reveals that $\Sigma_p/\dot{\Sigma}_p \propto r/v_r \propto r^{1-d}$. If we ignore corrections to v_r from the inertial slow-down effect and from turbulent stresses, then $d = d_{Ep} = p = 3/2$ for model H. Hence, $\Sigma_p/\dot{\Sigma}_p \propto r^{-1/2}$, the radial profile of Σ_p flattens with time, and planetesimal formation is triggered first at the outer boundary of the particle disk.

Figure 4 displays the evolution for nebular model Af, for which initial density profiles are shallower ($p = n = 1$) and temperature profiles are steeper ($q = 0.63$) than for model H. Both Epstein drag and turbulent stresses are included. Results that include only Epstein drag are similar and not shown in Figure 4 so as not to clutter it. This simulation was halted after 1.2×10^6 yrs when $\Sigma_p > \Sigma_{p,cr}$ at $r = 0.5$ AU, the inner boundary of the simulation domain. By contrast to model H, planetesimal formation begins at the inner edge of the
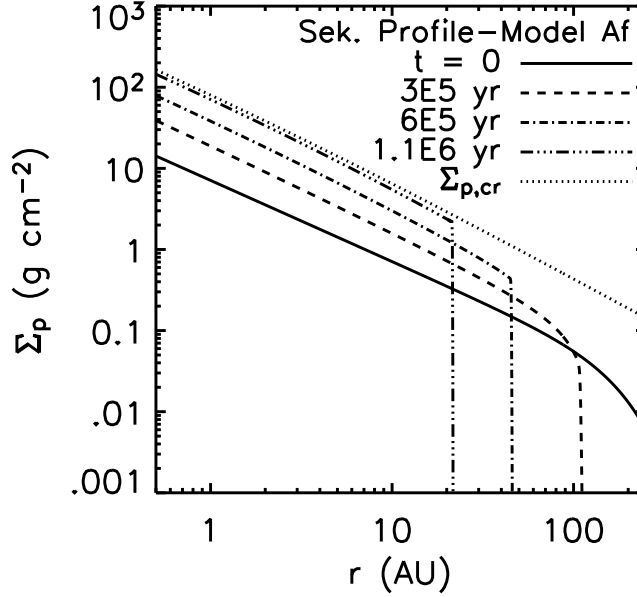
Fig. 4.— Similar to Figure 3, except for model Af ($p = n = 1$, $q = 0.63$). Epstein drag and turbulent stresses are included. The evolution proceeds relatively slowly for this model because the velocity index $d \approx d_{\mathrm{Ep}} = 0.87$ ($v_r \propto r^d$) is smaller than for model H ($d_{\mathrm{Ep}} = 1.5$), so that drift velocities are smaller for this model than for model H outside $r \sim 1$ AU. Since $d_{\mathrm{Ep}} < 1$, $\Sigma_{\mathrm{p}}(r)$ steepens and first exceeds $\Sigma_{\mathrm{p,cr}}$ at the inner boundary of the simulation, $r_{\mathrm{in}} = 0.5$ AU.

solid disk for model Af; the difference arises because $d = 0.87 < 1$ for the latter model, so that $\Sigma_{\mathrm{p}}/\dot{\Sigma}_{\mathrm{p}} \propto r^{+0.13}$ and the radial profile of particle surface density steepens (see the above discussion for model H).

3.3. Test Cases

To gain confidence in our numerical results and to aid in their interpretation, we ran two test cases that employ simplified prescriptions for the particle flux. Since these simple test cases do not depend on the detailed features of Sekiya's (1998) model, we can also gauge the degree to which our results are model-independent. These simple models allow $\Sigma_{\mathrm{p}} > \Sigma_{\mathrm{p,cr}}$ because they are constructed without regard to the physics of Kelvin-Helmholtz turbulence, and computationally they are less intensive.
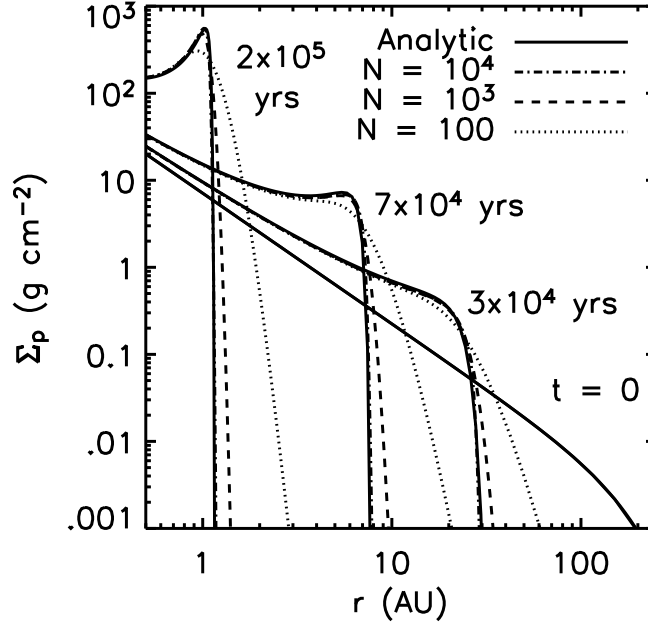
Fig. 5.— Demonstration that our numerical simulation converges to the analytic result of YS02, even when sharp density peaks are present. Inertial slow-down effects and turbulent stresses are ignored in this test case; their restoration would smooth away the density peaks seen here. The disk is described by model H with chondrule-like particles.

We first work in the limit of low particle density, $\rho_{\rm p} \ll \rho_{\rm g}$, and set the particle flux $F = F_{\rm Ep,ind} = \Sigma_{\rm p} v_{\rm Ep,ind}$. This expression was used by YS02 to obtain analytic solutions for the global evolution of particle surface density. We check our numerical code against these analytic solutions in Figure 5 at different grid resolutions. We chose model H because it gives rise to density cusps that provide more rigorous tests of numerical resolution than the smooth density profiles generated by model Af. The numerical solutions converge to the analytic result with increasing N_r; by $N_r = 10^4$, the analytic and numerical results are virtually indistinguishable. (In practice, for the more computationally intensive models that require root finding, we chose $N_r = 10^3$.)

Our other test case assumes that $\rho_{\rm p}$ is vertically constant within the particle layer. This "slab" approximation is a useful bridge between the low-density limit ($F = F_{\rm Ep}$) and the full treatment based on the Sekiya profiles. The vertically integrated fluxes due to Epstein drag and turbulent stresses under the slab approximation read, respectively,

$$\frac{F_{\rm Ep,slab}}{2\rho_{\rm g} H_{\rm p} v_{\rm Ep,ind}} = \frac{\sigma}{(1+\sigma)^2} \, , \tag{40}$$
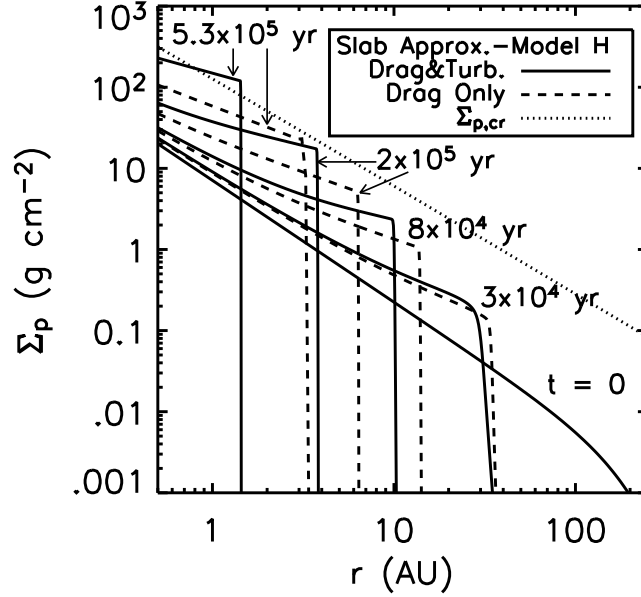
Fig. 6.— Similar to Figure 3, except ρ_{p} is assumed to be vertically constant within the particle layer. This "slab approximation" captures the salient features of the full treatment based on Sekiya's (1998) models, including inertial slow-down, turbulent speed-up, and the smoothing away of density peaks seen in Figure 5. This simulation employed $N_r = 10^3$ grid points.

$$\frac{F_{\mathrm{turb,slab}}}{2\rho_{\mathrm{g}}H_{\mathrm{p}}v_{\mathrm{Ep,ind}}} = \left(\frac{\sigma}{1+\sigma}\right)^2 , \tag{41}$$

where $\sigma \equiv \Sigma_{\mathrm{p}}/(2\rho_{\mathrm{g}}H_{\mathrm{p}})$. For comparison, in the limit of low particle density, $F_{\mathrm{Ep}}/(2\rho_{\mathrm{g}}H_{\mathrm{p}}v_{\mathrm{Ep}}) = \sigma$ increases without bound with increasing Σ_{p}. In the slab treatment, accounting for the effect of inertial slow-down saturates the flux to values below F_{Ep} for $\sigma \gtrsim 1$.

Figure 6 portrays the evolution of particle surface density in nebular model H under the slab approximation. The evolution is remarkably similar to that displayed in Figure 3. In generating Figure 6, we have taken $H_{\mathrm{p}} = \sqrt{Ri}\eta r = \eta r/2$. In both Figures 3 and 6, the density peaks seen in Figure 5 are smoothed away in similar fashion. Smoothing occurs because of flux saturation in regions where $\sigma \gtrsim 1$. Under the slab approximation, turbulent stresses alter the evolution of particle density more markedly than under the full treatment; however, it remains the case qualitatively that turbulent stresses abet particle pile-ups.

Note that the particle pile-up occurs relatively quickly in Figure 5, while the evolutions shown in both Figures 3 and 6 evince similar degrees of inertial slow-down. The slow-down is
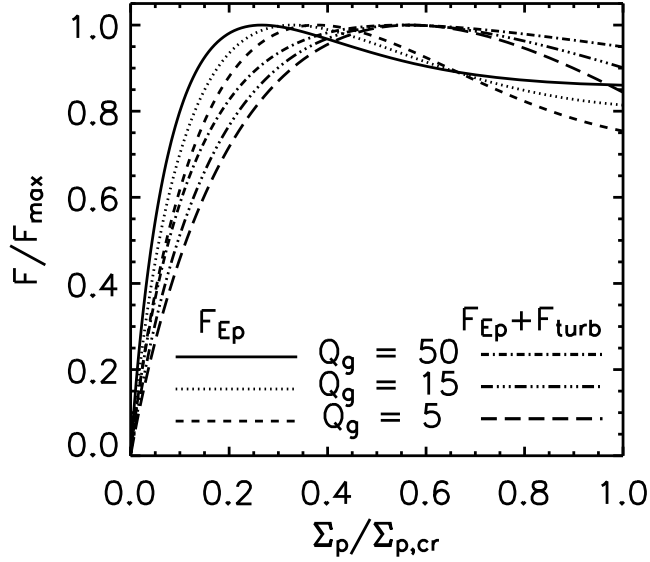
Fig. 7.— Vertically integrated, radial particle fluxes versus Σ_p based on Sekiya's (1998) profiles. Results are shown for gas drag with and without turbulent stresses for several values of Toomre's Q parameter for the gas, Q_g. Instabilities can occur where $\partial F/\partial \Sigma_p < 0$.

most pronounced under the full treatment using the Sekiya profiles. These differences arise from the fact that the integral in (32), when performed at fixed Σ_p, diminishes either when H_p decreases or when $\rho_p(z)$ becomes more inhomogeneous.

One qualitative difference arises between using the slab approximation and the Sekiya models. In the former case, the radial particle flux monotonically increases with Σ_p and asymptotes to a constant value. In the latter case, the flux attains a global maximum at $\Sigma_p \approx 0.6\Sigma_{p,cr}$, if turbulent stresses and Epstein drag are included. The maximum occurs at lower Σ_p if only Epstein drift is considered. This turnover of the flux is shown in Figure 7. At $\Sigma_p > 0.6\Sigma_{p,cr}$, the flux decreases with increasing Σ_p. The magnitude of this decrease depends on the strength of self-gravity of the gas, as measured by the parameter $Q_g = 4/(\sqrt{2\pi}\psi)$. Smaller values of Q_g indicate stronger self-gravity and cause a larger drop in the flux. The turn-over occurs because as Σ_p approaches $\Sigma_{p,cr}$, H_p decreases and engenders greater inertial slow-down. In addition, as Σ_p increases, larger amounts of solids are swallowed into the cusp in density near the midplane, where the inertial slow-down effect is greatest. Both of these behaviors of $\rho_p(z)$ with Σ_p can be seen in Figure 1 of YS02.

The turn-over in F versus Σ_p can spur instabilities. Imagine that $\partial F/\partial \Sigma_p < 0$ and that a region of high Σ_p exists downstream of a region of low Σ_p. The low-density region

transmits a comparatively large flux to the high-density region, while the high-density region parts with a comparatively small flux. The high-density region therefore amplifies its density, at the expense of regions yet further downstream. In this way, the instability propagates downstream. Indeed, we believe that this instability manifested itself in our simulations in the form of a "saw-tooth" where the density fluctuated from one radial grid point to the next. The saw-tooth typically appeared when $\Sigma_{\rm p}/\Sigma_{\rm p,cr} \gtrsim 0.8$—0.9, in the regime where $\partial F/\partial \Sigma_{\rm p} < 0$. Attempts to resolve the instability at higher grid resolutions were unsuccessful; more study is needed.[3] While the shape of the F-$\Sigma_{\rm p}$ relation that we have computed raises the possibility that the effective saturation criterion should instead read $\Sigma_{\rm p} > 0.6\Sigma_{\rm p,cr}$, such a refinement may not be important in practice. If aerodynamic drift (and other mechanisms) can raise $\Sigma_{\rm p}$ to within a factor of 2 of $\Sigma_{\rm p,cr}$, they are likely to raise it all the way.

4. On the Validity of Plate Drag

In §2.2.2 and §3 we treated turbulent stresses without recourse to the plate drag approximation. Since the plate drag formulae are commonly employed in the literature, we explain here why we believe that their use is problematic at best and inappropriate at worst.

We have already mentioned in §2.2.1 the large range of values that the critical parameter, Re*, has historically taken and the difficulty in determining its true form. More fundamentally, the plate drag approximation begs the question of whether we can think of a slurry of particles as a monolithic entity. GP00 propose that such collective behavior is possible if wakes around particles overlap, analogous to the practice of "drafting" in bicycle racing. In the present context of the Epstein drag regime, these wakes are disturbances having tiny length scales in the free molecular flow. If one assumes that each solid particle leaves a "footprint" on the surrounding fluid flow that extends a distance of order the gas mean free path, λ, then one can show that for $\rho_{\rm p} \sim \rho_{\rm g}$ the probability that another particle lies within this sphere of influence is $\sim 10^{-8}$.

Despite the failure of free molecular wakes to overlap, collective effects among solids are not precluded. Indeed, the "inertial slow-down" correction to the particle drift velocity [equation (7)] tells us that particles are well aware of each other if their collective density, $\rho_{\rm p}$, approaches $\rho_{\rm g}$. This communication arises when one accounts for the back-reaction of particles dragging on gas. We find that this effect describes most of the collective behavior of solids, even when turbulent stresses, which are also collective in nature, are included.

---

[3]One could perform a local stability analysis analogous to that carried out by GP00. This would require restoring the time derivatives to our momentum equation (18).

Thus, plate drag overestimates turbulent stresses. Our final criticism concerns the assumption inherent in the plate drag approximation that the particle-dominated midplane behaves as a geometrically thin Ekman layer. We proceed to show that the turbulent diffusivity in such an Ekman layer is so large that the particle layer cannot be as thin as assumed.

Ekman boundary layer theory applies to a medium having viscosity ν_{Ek} and rotating at frequency Ω, and assumes that other physics (e.g., buoyancy) is negligible. The height of the Ekman layer is

$$H_{\mathrm{Ek}} \approx \sqrt{\nu_{\mathrm{Ek}}/\Omega}\,. \tag{42}$$

The viscosity, ν_{Ek}, which cannot be directly measured in protoplanetary disks, is defined in terms of H_{Ek} and the critical Reynolds number,

$$\mathrm{Re}^* \equiv \frac{H_{\mathrm{Ek}}\eta v_K}{\nu_{\mathrm{Ek}}}\,, \tag{43}$$

where the characteristic velocity difference across the boundary layer is $\Delta v_\phi \approx \eta v_K$. From equations (42) and (43), we derive the turbulent diffusivity of the layer,

$$\nu_{\mathrm{Ek}} \sim \frac{\eta^2 r v_K}{(\mathrm{Re}^*)^2}\,, \tag{44}$$

where all quantities, including the critical parameter Re^*, are assumed to be known. The corresponding thickness of the Ekman layer is

$$H_{\mathrm{Ek}} \sim \frac{\eta r}{\mathrm{Re}^*}\,. \tag{45}$$

Equations (42)–(45) are standard in the literature (e.g., Goldreich & Ward 1973; Dobrovolskis et al. 1999; GP00).

We compare H_{Ek} to the thickness of the particle layer that is stirred by turbulence characterized by ν_{Ek}. Equation (27) with $\nu_z = \nu_{\mathrm{Ek}}$ yields, to order-of-magnitude, this thickness[4]:

$$H_{\mathrm{Ek,stir}} \sim \sqrt{\frac{\nu_{\mathrm{Ek}}}{\Omega^2 t_{\mathrm{stop}}}} \sim \frac{H_{\mathrm{Ek}}}{\sqrt{\Omega t_{\mathrm{stop}}}}\,. \tag{46}$$

---

[4]The assumption from § 2.2.2 that $Sc \approx 1$, true for $\Omega t_{\mathrm{stop}} \ll 1$, is still in effect.

Whenever $\Omega t_{\mathrm{stop}} \ll 1$, $H_{\mathrm{Ek,stir}}$ is inconsistently larger than H_{Ek}. GP00 appreciate this point (see their equation [14]) and conclude that the plate drag formula yields self-consistent results for particles large enough (i.e., $a \sim 10$ cm at $r \sim 1$ AU) that $\Omega t_{\mathrm{stop}} \sim 1$. If, however, $\Omega t_{\mathrm{stop}} \ll 1$, then a layer as thin as H_{Ek} will be stirred thicker until vertical shear becomes too weak to stir it further. This is the marginally Kelvin-Helmholtz turbulent state that we have employed throughout this paper.

It should not be too surprising that the turbulent boundary layer as pictured within the plate drag approximation cannot, in general, be accurately described as an Ekman layer. The large Rossby number of the layer,

$$\mathrm{Ro} \equiv \frac{\Delta v_\phi}{\Omega H_{\mathrm{Ek}}} \approx \mathrm{Re}^* \gg 1 \,, \tag{47}$$

implies that inertia is more significant than rotation. Vertical shear and buoyancy are important ingredients missing from the traditional Ekman layer description. The Kelvin-Helmholtz turbulent layer that we have considered has $\mathrm{Ro} \sim 1$. Recent work by Ishitsu & Sekiya (2003) suggests that centrifugal and Coriolis forces weaken vertical shear instabilities. This finding only helps to further pave the way for planetesimal formation by gravitational instability. See Appendix A for further discussion of rotational effects on particle drift rates.

Finally, we comment that the Ekman layers in the Earth's atmosphere are not subject to the crisis described here. In the Earth's case, atmospheric shear is generated by thermal forcing, which is unaffected by boundary layer turbulence. By contrast, vertical shear in protoplanetary disks is generated by the inertia of particles within the boundary layer.

In conclusion, in the small particle limit where $\Omega t_{\mathrm{stop}} \ll 1$, the plate drag formula seems to apply only if particles were effectively glued onto a fixed plate!

5.   Summary

We have investigated radial drift rates of solid particles within protoplanetary disks that derive their turbulence from vertical shear near their strongly stratified midplanes. Previous models by YS02 calculate drift rates according to mean flow differences between the sub-Keplerian gas and the more nearly Keplerian particles. We improve on their work by incorporating the effects of collective particle inertia [equation (7)] and the contribution to particle accretion from turbulent stresses [equation (29)]. These turbulent stresses are calculated in a physically self-consistent manner; turbulent particle diffusivities are derived from the detailed balance of vertically upward and downward particle fluxes within states of marginal Kelvin-Helmholtz turbulence [as computed by Sekiya (1998)]. Our results reinforce

the conclusions of YS02 that particle drifts lead to particle pile-ups. These pile-ups become sites of planetesimal formation by gravitational instability once the surface density of solids exceeds the saturation limit. We have explained why turbulent stresses cannot be modeled using the traditional plate drag approximation in the (most interesting) limit of small particle size; our alternative approach leads us to conclude that turbulent stresses hasten particle pile-ups.

Inertial slow-down—the diminishing ability of gas to frictionally sap the angular momentum of particles as the particle mass density increases above the gas mass density—resulted in longer accretion timescales and a more even spreading of solids over larger regions of space, as compared to the results of YS02. Inclusion of this effect delays the particle pile-up, but only mildly.

How the story of planetesimal formation unfolds in actual circumstellar disks will depend on a variety of factors in addition to aerodynamic drift of solids. Photoevaporation by stellar ultraviolet photons and stellar winds will strip gas from the disk surface and leave solids near the midplane. Furthermore, a distribution of particle sizes and geometries (fluffy vs. compact) will smooth particle surface density profiles.

Is planetesimal formation triggered first near the outer or inner edges of accreting particle disks? The answer bears directly on the architecture of planetary systems, on whether the mass in a planetary system is weighted toward small stellocentric distances (as they seem to be in extrasolar systems possessing Jovian-mass planets inside $r \sim 1$ AU) or larger stellocentric distances (as they are in our solar system). We have quantified the question of inside-out versus outside-in planet formation in terms of the index, d, which describes the inward radial drift speed of particles ($v_r \propto r^d$). If $d > 1$, then particle pile-ups occur first at the outer edge of the particle disk. For our power-law disks, $d \simeq d_{\mathrm{Ep}} = p - q + 1/2$, where p and q describe the variation of gas surface density and temperature with disk radius, respectively. Our knowledge of these quantities is informed by observations of circumstellar disks at mid-infrared to millimeter wavelengths. To date, q-values near 0.5 seem difficult to avoid (see, e.g., Chiang et al. 2001; D'Alessio et al. 2001), while estimates for p-values via dust continuum observations are traditionally hampered by lack of spatial resolution and ignorance concerning the dust opacity and the dust-to-gas ratio. Improvements in spatial resolution are promised by future detectors such as the Stratospheric Observatory for Infrared Astronomy (SOFIA) and the Atacama Large Millimeter Array (ALMA), while direct measurements of molecular hydrogen gas are possible via its rotational transitions at wavelengths of 17 and 28 μm (e.g., Thi et al. 1999) and its ro-vibrational lines at 2.1 μm (e.g., Bary et al. 2003).

As noted by YS02, observations of our solar system's Kuiper Belt point with ever in-

creasing conviction to the existence of a hard outer edge to the classical Kuiper Belt at $r \approx 48$ AU (e.g., Allen et al. 2002, and references therein). Were it not for the coincidence of the edge with the location of the 2:1 mean-motion resonance with Neptune, we might simply ascribe this edge to a particle pile-up and the necessity of exceeding a critical threshold metallicity for planetesimal formation. We therefore offer a slightly more complicated scenario to explain these observations. A hard, primordial edge to the solar system formed at $r < 48$ AU as a consequence of the processes described in YS02 and this work. As Neptune was scattered (stochastically) outward by planetesimal encounters (Fernandez & Ip 1984; Hahn & Malhotra 1999), its exterior resonances captured bodies and carried them to greater heliocentric distances (Malhotra 1995; Chiang & Jordan 2002). In this way, the 2:1 (strongest, outermost) Neptunian resonance combed the primordial edge outward to its present location.

A. Modifications to Turbulent Drift Rates by Rotation

We have modeled Kelvin-Helmholtz turbulence as occurring in a vertical, Cartesian shear flow, without regard to the Coriolis force. This force deflects turbulent eddies in the z-ϕ plane into the r-ϕ plane and thereby introduces a non-zero $P_{r\phi}$ stress into equation (18) for particle drift rates. Here we justify the neglect of this term, $(1/r^2)\partial(r^2 P_{r\phi})/\partial r$, as compared to $\partial P_{z\phi}/\partial z$. Since the Rossby number of the turbulent layer is of order unity,

$$\text{Ro} = \frac{\Delta v_\phi}{\Omega H_{\rm p}} \sim \frac{\eta v_K}{\Omega \eta r} \sim 1 \,, \tag{A1}$$

the magnitude of $P_{r\phi}$ is the same as that of $P_{z\phi}$. An equivalent way of seeing this is to write down an expression for $P_{r\phi}$ analogous to equation (24),

$$P_{r\phi} = \rho \nu_r \frac{\partial v_\phi}{\partial r} \sim \rho \nu_r \frac{\Omega r}{r} \sim \rho \nu_r \Omega \,, \tag{A2}$$

which is of the same order as

$$P_{z\phi} = \rho \nu_z \frac{\partial v_\phi}{\partial z} \sim \rho \nu_z \frac{\eta v_K}{\eta r} \sim \rho \nu_z \Omega \,, \tag{A3}$$

since $\nu_r \sim \nu_z$. Then it is clear that $(1/r^2)\partial(r^2 P_{r\phi})/\partial r \sim P_{r\phi}/r$ is smaller than $\partial P_{z\phi}/\partial z \sim P_{z\phi}/H_{\rm p}$ by $\sim H_{\rm p}/r \sim \eta \ll 1$.

B.   Required Levels of Disk Passivity

This appendix quantifies the extent to which circumstellar disks must be passive for the processes described in this paper to occur. Here we are considering "anomalous" sources of turbulence and angular momentum transport not arising from vertical shear in stratified particle layers (e.g., the magneto-rotational instability). We first ask under what conditions radial accretion velocities arising from an anomalous viscosity exceed the particle accretion velocities derived in this paper. For the latter we employ $v_{\rm Ep}$ (since $v_{\rm r,turb} < v_{\rm Ep}$), and for the former we employ the usual α-prescription,

$$v_\alpha \sim \alpha_r \eta v_K \,, \tag{B1}$$

where α_r parameterizes the strength of radial transport of angular momentum. Then one necessary criterion for disk passivity reads

$$\alpha_r \ll \frac{\rho_{\rm g}}{\rho} \Omega t_{\rm stop} \,. \tag{B2}$$

For chondrule-like particles at $r \sim 1$ AU in the MMSN, this criterion is satisfied for disks with $\alpha_r \ll 10^{-4}$. It could be satisfied in more active disks for larger particles or at larger disk radii.

A second criterion demands that the disk be sufficiently quiescent to permit vertical settling of solids. From equation (27), we estimate the diffusivity generated by Richardson turbulence as $\nu_z \sim (\eta v_K)^2 t_{\rm stop}$, where we have used $H_{\rm p} \sim \eta r$. We express this diffusivity in terms of an α-viscosity as $\alpha_z \equiv \nu_z \Omega/c_g^2$, where the subscript z reminds us that turbulence need not be isotropic. Then this second criterion requires that any additional source of turbulence apart from vertical shear be characterized by

$$\alpha_z \lesssim \Omega t_{\rm stop} \,. \tag{B3}$$

For our power-law disks containing millimeter-sized particles, this criterion reads $\alpha_z \lesssim$

$10^{-7} (r/\mathrm{AU})^{1+\mathrm{p}-\mathrm{q}}$. For model H, $1 + p - q = 2$. The most stringent requirements on disk passivity lie at small stellocentric distances.

We note that $\alpha_z < 10^{-7}$ is still well satisfied by molecular viscosity, for which $\alpha_r \sim \alpha_z \sim \lambda/H_\mathrm{g} \sim 10^{-12}$ at $r \sim 1$ AU.

Does the anomalous viscosity ever shut off? Observations of T Tauri stars (and young brown dwarfs) indicate that infrared excesses indicating the presence of disks almost always correlate with Hα emission and other accretion signatures (Kenyon & Hartmann 1995; Liu et al. 2003). However, this oft-cited correlation has a considerable amount of scatter. Figure 4 of Kenyon & Hartmann 1995 clearly shows that a sizable fraction of systems with infrared excesses have small Hα equivalent widths. These may represent disks that are quiescent enough to form planetesimals. We note that accretion signatures at optical-to-ultraviolet wavelengths pertain to activity in the immediate vicinity of the star; they may implicate accretion within $\sim$30 stellar radii of the stellar surface, but they are not diagnostic of conditions at much greater stellocentric distances. Furthermore, evidence for significant vertical settling of dust in disk photospheres and the implied absence of vertical stirring in the uppermost scale heights is presented by Chiang et al. (2001), based on modeling mid–to–far infrared fluxes of Herbig Ae systems.

In principle, it is possible for disks to exhibit $\alpha_r \gg \alpha_z$ and to thereby reconcile modest levels of accretion with vertical settling of solids and particle pile-ups. For weakly viscous flows having small Rossby number, the Taylor-Proudman theorem constrains rotating flow to be two dimensional, parallel to the midplane, with no variation of velocity with height z (Pedlosky 1987, p. 43). Indeed, in both the Earth's atmosphere and the Earth's oceans, the ratios of horizontal to vertical viscosities are roughly estimated to be $\sim$$10^4$ (Pedlosky 1987, p. 185). By analogy to our problem, we could simultaneously demand $\alpha_z \sim 10^{-8}$ so as to allow vertical settling and $\alpha_r \sim 10^{-4}$ so as to yield observable accretion rates of $\dot{M} \sim 10^{-9}$–$10^{-8} M_\odot/\mathrm{yr}$ while not violating (B2) throughout most of the disk. Thus, mildly accreting class II protostellar systems could well be sites of planetesimal formation via gravitational instability.

REFERENCES

Allen, R. L., Bernstein, G. M., & Malhotra, R. 2002, AJ, 124, 2949

Balbus, S. A., & Hawley, J. F. 1991, ApJ, 376, 214

Bary, J. S., Weintraub, D. A., & Kastner, J. H. 2003, ApJ, 586, 1136

Blum, J., & Wurm, G. 2000, Icarus, 143, 138

Chiang, E. I. 2003, in ASP Conf. Ser., Astrophysics of Dust, ed. G. Clayton, B. Draine, & A. Witt, (San Francisco: ASP), in press

Chiang, E. I., & Goldreich, P. 1997, ApJ, 490, 368

Chiang, E. I., & Jordan, A. B. 2002, AJ, 124, 3430

Chiang, E. I., Joung, M. K., Creech-Eakman, M. J., Qi, C., Kessler, J. E., Blake, G. A., & van Dishoeck, E. F. 2001, ApJ, 547, 1077

Cuzzi, J. N., Dobrovolskis, A. R., & Champney, J. M. 1993, Icarus, 106, 102

D'Alessio, P., Calvet, N., & Hartmann, L. 2001, ApJ, 553, 321

Dobrovolskis, A. R., Dacles-Mariani, J. S., & Cuzzi, J. N. 1999, J. Geophys. Res., 104, 30805

Fernandez, J. A., & Ip, W.-H. 1984, Icarus, 58, 109

Gammie, C. F. 2001, ApJ, 553, 174

Goldreich, P., & Ward, W. R. 1973, ApJ, 183, 1051

Goodman, J., & Pindor, B. 2000, Icarus, 148, 537

Hahn, J. M., & Malhotra, R. 1999, AJ, 117, 3041

Hayashi, C. 1981, Prog. Theor. Phys. Suppl., 70, 35

Ishitsu, N., & Sekiya, M. 2003, Icarus, 165, 181

Kenyon, S. J., & Hartmann, L. 1995, ApJS, 101, 117

Liu, M. C., Najita, J., & Tokunaga, A. T. 2003, ApJ, 585, 372

Malhotra, R. 1995, AJ, 110, 420

Nakagawa, Y., Sekiya, M., & Hayashi, C. 1986, Icarus, 67, 375

Pedlosky, J. 1987, Geophysical Fluid Dynamics, 2nd edn. (New York: Springer-Verlag)

Press, W. H., Teukolsky, S. A., Vetterling, W. T., & Flannery, B. P. 1992, Numerical recipes in C. The art of scientific computing (Cambridge: University Press)

Sekiya, M. 1998, Icarus, 133, 298

Thi, W., van Dishoeck, E. F., Blake, G. A., van Zadelhoff, G., & Hogerheijde, M. R. 1999, ApJ, 521, L63

Weidenschilling, S. J. 1995, Icarus, 116, 433

—. 2003, Icarus, 165, 438

Weidenschilling, S.J., & Cuzzi J.N. 1993, in Protostars and Planets III, eds. E.H. Levy and J.I. Lunine (Tucson: University of Arizona Press), 1031–1060

Wurm, G., Blum, J., & Colwell, J. E. 2001, Icarus, 151, 318

Youdin, A. N., & Shu, F. H. 2002, ApJ, 580, 494